Clays and Clay Minerals, Vol. 46, No. 1, 27–37, 1998.

LOW-TEMPERATURE ALTERATION IN TUFFS FROM YUCCA MOUNTAIN, NEVADA

JILLIAN F. BANFIELD† AND WILLIAM W. BARKER

Department of Geology and Geophysics, University of Wisconsin–Madison, 1215 W Dayton St., Madison, Wisconsin 53796

Abstract—The structure, chemistry and distribution of hydrothermal alteration and weathering products of feldspars and glass in 3 samples of Yucca Mountain tuffs (GSW G4 borehole at a depth of 1531 ft (464 m) and USW GU3 borehole at 1406 ft (426 m) from the Calico Hills Formation and USW G4 at a depth of 272 ft (82.4 m) from the Topobah Springs Member) were examined by high-resolution transmission electron microscopy (HRTEM) and analytical electron microscopy (AEM). Alteration products are of interest because they may influence the form and distribution of contaminants released from the proposed high-level nuclear waste repository. Samples from the Calico Hills Formation contain alkali-bearing aluminosilicate glass and its alteration products. Zeolites appear to have formed from compositionally similar glass by recrystallization, probably under hydrothermal conditions. Crystals are fibrous and frequently no more than a few tens of nanometers in diameter. Porous aggregates of few-nanometer-diameter, poorly crystalline silica spheres (probably opal C-T) develop adjacent to corroded glass surfaces and zeolite crystals. Finely crystalline Fe-rich smectites coat etched glass surfaces, zeolites and feldspar crystals and occur within opal-like silica aggregates. Microstructures in the clay-dominated coatings and details of smectite–glass interfaces suggest that clays grow in orientations controlled by heterogeneously retreating surfaces and from constituents released at associated glass dissolution sites. The alteration assemblage also includes finely crystalline hematite, goethite, Mn-oxide films and illite formed by alteration of muscovite. The zeolitized sample contains abundant opal-like silica whereas glass in the unzeolitized sample is weathered to smectite-like clays. These differences may be attributed to hydrological and consequent geochemical factors resulting from the higher porosity of zeolitized samples. Exsolved alkali feldspar, which occurs as micron-sized crystals in the Calico Hills Formation and as phenocrysts and in the groundmass of the devitrified Topobah Springs Member, are almost unaltered. Feldspar alteration is confined to cracks and grain boundaries, where minor, poorly crystalline, Fe-bearing aluminosilicate alteration products are developed. In these tuffs, most of the porosity, permeability, high surface area and capacity to affect solution chemistry are associated with products of glass alteration.

Key Words—Alteration, Clays, Coatings, Glass, Silica, Smectite, Tuff, Weathering, Yucca Mountain, Zeolites.

INTRODUCTION

Yucca Mountain is the proposed site for the United States high-level nuclear waste repository. Considerable research has been conducted in order to understand the mineralogy of Yucca Mountain tuffs, to predict their ability to affect solution chemistry and solute transport and to understand how they will be modified by thermal and hydrologic changes associated with proximity to the repository site. Effort devoted to understanding adsorption of radionuclides and other potential contaminants by the phases (Thomas 1987) in the tuffs highlighted the need for a high-resolution microscopy study of secondary products. Research presented in this paper was undertaken to investigate the form and distribution of finely crystalline and non-crystalline alteration products in these rocks and to attempt to understand the processes leading to their formation.

Previous work on the mineralogy of the Yucca Mountain tuffs and their fracture coatings employed X-ray diffraction (XRD), scanning electron microscopy (SEM) and electron microprobe (EMP) analysis. The 3-dimensional distribution of minerals in Yucca Mountain rocks, including samples from core close to the samples characterized in this study, were described by Broxton et al. (1985, 1987), Chipera and Bish (1989) and Bish and Chipera (1989). Chipera and Bish (1989) reported that the 75–500 μm fraction of G4 1502, a sample from 8.8 m above G4 1531 (examined in this study), contained about 2% smectite, 71% clinoptilolite, 4% quartz, 15% opal CT and 3% K-feldspar. Experimental data, including cation exchange capacity (CEC) and adsorption results for Am, Np, Pu, Sn and Tc for G4 1502, were reported by Thomas (1987). Bish and Chipera (1989) describe G4 1544, a sample from 3.96 m below G4 1531 (examined in this study), as containing about 3% smectite, 50% clinoptilolite, 20% mordenite, 6% quartz and 12% cristobalite. Whole-rock chemistry for G4 1544C was reported by Broxton et al. (1987). Sample GU3 1436, a sample from 9.14 m below GU3 1406 (examined in this

† Current Address: Graduate School of Science, Mineralogical Institute, University of Tokyo, Hongo, Bunkyo-ku, Tokyo 113, Japan.

study), was reported to contain traces of smectite and mica, about 4% quartz, 3% opal CT, 18% K-feldspar and about 75% glass, whereas GU3 1415, from 2.74 m below GU3 1406, contained approximately 5% quartz, 6% cristobalite, 35% K-feldspar and 55% glass (Bish and Chipera 1989).

The densely welded, devitrified Topobah Springs member of the Paintbrush tuff is the candidate host rock for the repository (Bolivar et al. 1989). Sample G4 268, a sample from 1.22 m above G4 272 (examined in this study), is reported to contain about 1% mica, 20% tridymite, 6% cristobalite, and 73% alkali feldspar (Bish and Chipera 1989). All 3 core samples examined in our work are from above the static water zone, which currently occurs at 545 m in the G4 borehole (Carlos et al. 1995; the water table is between 200 and 400 m below the potential repository; Bolivar et al. 1989).

XRD data provide useful information about tuff mineralogy. However, XRD data do not provide extremely important spatial and fine-scale structural information. This paper reports the first HRTEM and AEM data for 3 tuff samples selected for their importance to parallel adsorption studies conducted by researchers at Los Alamos National Laboratory (work in preparation).

Many studies have indicated that secondary minerals play important roles in controlling metal and organic adsorption and thus, solution chemistry and contaminant transport (for example, Coston et al. 1995). However, the nature of the fine-grained phases that make up these coatings and the mechanisms by which they form are poorly understood because of their chemical and structural complexity. This study describes coatings on glass, zeolites and feldspar and provides insights into the role of reactive surfaces in controlling nucleation and growth of secondary minerals in tuffaceous rocks. Although the research was focused by specific needs associated with the Yucca Mountain project, the results should be of more general interest because of the insights they provide into the nature of low-temperature alteration of tuffaceous rocks.

SAMPLES AND TECHNIQUES

Three samples of Yucca Mountain tuffs were provided to us by researchers at Los Alamos National Laboratory. Two samples from GSW G4, a borehole in the northeastern part of the proposed repository site, were from depths of 272 ft (82.4 m) (Topobah Spring Member) and 1531 ft (464 m) (Calico Hills Formation). The third core sample was from USW GU3, a borehole about a mile south of the proposed repository site. The sample from USW GU3 from 1406 ft (426 m) below the surface belongs to the Calico Hills Formation.

Tuff samples were epoxy-impregnated and petrographic thin sections mounted with acetone-soluble adhesive were prepared. Thin sections were reimpregnated with low-viscosity 2-part epoxy (M Bond) during polishing to <30-μm thickness as needed to prevent disaggregation. Barker and Banfield (1996) explain this sample preparation technique in detail. Areas of interest identified using polarized light microscopic examination with a Leica DMRX compound microscope were cut from thin sections, mounted on copper grids and Ar-ion-milled to electron transparency. These samples were C-coated and viewed in a Philips CM200 UT HRTEM operating at 200 kV. All electron micrographs were recorded at close to Scherzer defocus. Phases were identified using a combination of selected area electron diffraction (SAED), direct measurement of interplanar spacings in high-resolution images and chemical composition. AEM analyses were collected from submicron-diameter areas of minerals using a Noran energy dispersive X-ray (EDS) light element detector with a germanium crystal and Norvar thin window.

RESULTS

G4 1531 Calico Hills Formation

HRTEM images reveal that aluminosilicate glass is commonly highly etched and partially converted to domains of subparallel, fibrous, zeolite crystals (Figure 1). Although we did not measure porosity and permeability of bulk samples, TEM images clearly indicate that there is abundant open space associated with zeolitized areas. Pores in etched glass vary considerably in size. TEM data show they are commonly elongate, generally less than 50 nm wide and range up to a fraction of a micron in length (Figures 1, 2 and 3). A continuum between irregularly etched, noncrystalline glass (lower right of Figure 1b) and crystalline zeolites (upper right of Figure 1a and upper left of Figure 1b) was seen in this sample.

Zeolites and aggregates of small particles partially replace etched glass (Figure 2). Particle aggregates are very Si-rich with small, variable Al and K contents. Individual poorly crystalline or amorphous particles within these aggregates are typically a few to a few tens of nanometers in diameter. In some areas, individual particles adhere to zeolite surfaces and aggregates of particles fill spaces between clusters of zeolite crystals (Figure 3). Clay minerals with a basal spacing of 1 nm coat some zeolite surfaces (Figure 4). Clays develop with their c^* direction normal to the long axis of zeolite fibers. These coatings may be only a few nanometers in thickness (Figure 4).

Approximately spherical silica particles with a diameter of 10–15 nm are distributed in a relatively randomly packed arrangement (Figure 5). Very long, thin, clay laths occur throughout this material. These clays

https://doi.org/10.1346/CCMN.1998.0460104 Published online by Cambridge University Press

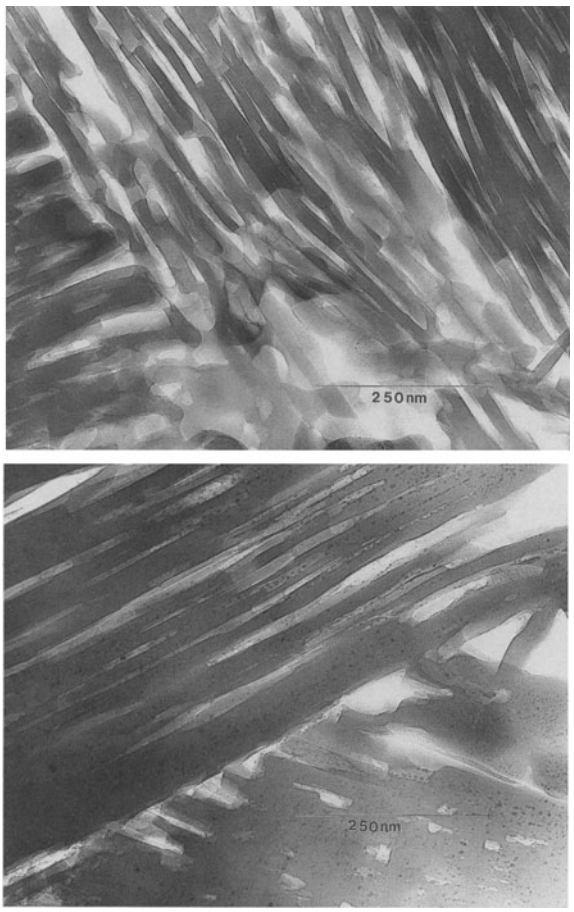

Figure 1. a) TEM of sample G4 1531 showing an apparent continuum from etched glass to crystalline elongate zeolites. b) Area similar to (a) at higher magnification. Note the large amount of <50-nm-diameter porosity.

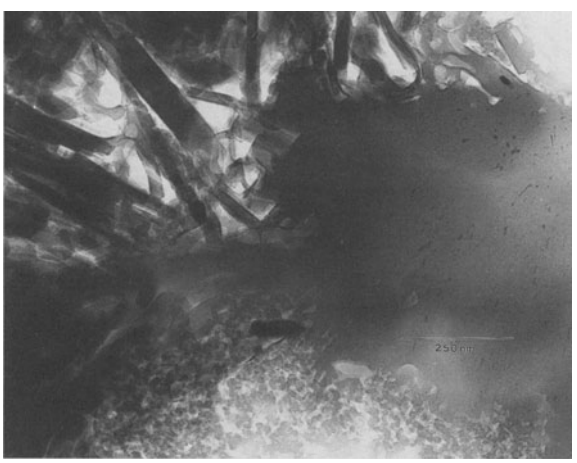

Figure 2. TEM of glass (center and right) and reaction products in sample G4 1531. Secondary minerals include elongate zeolite crystals, aggregates of about 10-nm-wide poorly crystalline silica particles, probably opal C-T (center bottom), minor smectite and Fe-oxides and oxyhydroxides (dark crystals).

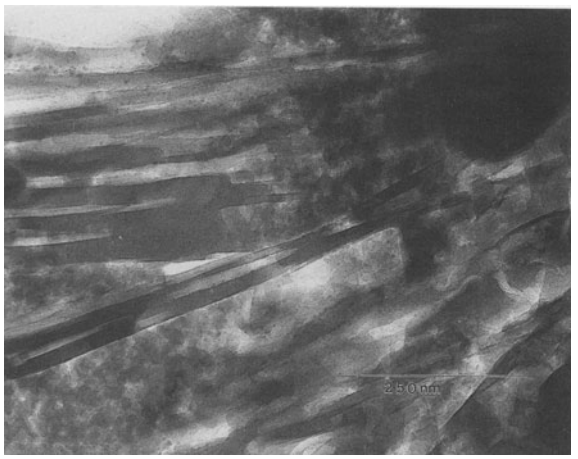

Figure 3. TEM showing a mixture of glass, zeolites (needle-shaped and tabular crystals with dark contrast) and semi-spherical opal-like silica (center top and bottom left) in sample G4 1531.

are commonly no more than a couple of unit cells thick, though they may range up to more than 10 nm (10 unit cells) in some areas (center of Figure 5).

Sample G4 1531 also contains small groundmass K-rich feldspars (Figure 6), often surrounded by glass. The feldspars display tweed textures (microcline twinning). Although surrounded by abundant products of diagenetic alteration and weathering of glass, these K-feldspar crystals are essentially unweathered.

GU3 1406 Calico Hills Formation

GU3 1406 also contains abundant etched and partially altered glass. Clays and minor Fe- and Mn-oxides and oxyhydroxides dominate the alteration assemblage. Complex mixtures of glass and wavy aggregates

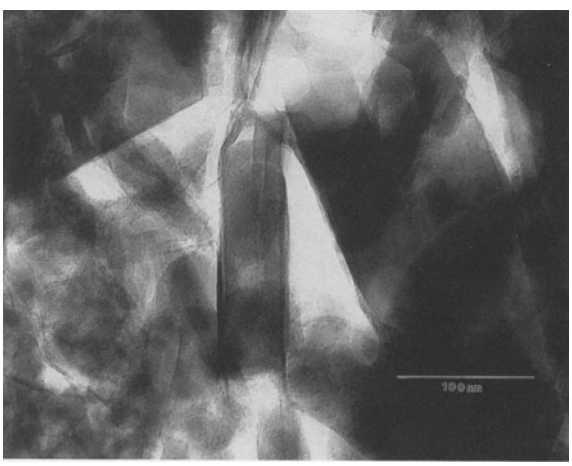

Figure 4. TEM showing zeolites (center and top) and opal-like silica (lower left) in sample G4 1531. Note the surfaces of the near-vertical zeolite needle at the center of the image are coated by few-nanometer-thick smectite layers.

https://doi.org/10.1346/CCMN.1998.0460104 Published online by Cambridge University Press

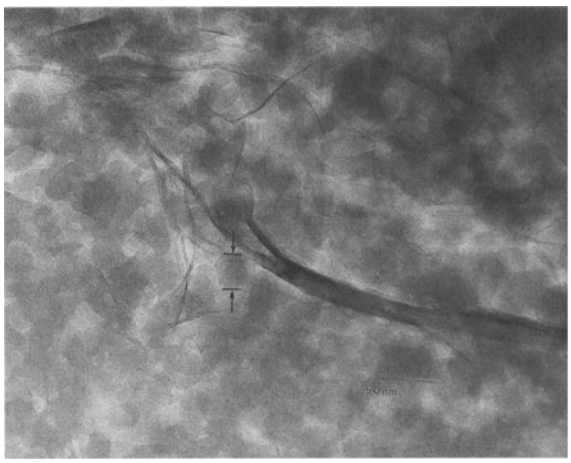

Figure 5. Higher-resolution TEM image of few unit cell wide smectite-like clays crystallized (curved, dark strips) within opal-like silica aggregates (consisting of ~13-nm-diameter rounded particles, see arrows) adjacent to corroded glass surfaces (sample G4 1531).

Figure 7. TEM showing wavy smectite-like clays (possibly smectite, possibly with some illite) growing out from corroded glass (even contrast area at bottom center) surfaces in sample GU3 1406.

of clays with a complex chemistry and 1-nm basal spacing characterize large regions of this sample (Figure 7). In some areas, glass contains numerous, rounded solution pits rimmed by these clays (Figure 8).

Some glass surfaces are in intimate contact with complex clay coatings. Figure 9 shows a coating consisting of a layer silicate with a 1-nm basal spacing and disordered stacking (also see inset SAED pattern in Figure 9) and oriented elongate crystals of an Fe-rich phase. Clays grow with their basal planes parallel to the glass surface and layers terminate against walls of etch pits in the surface (Figure 9).

Clays in adjacent pits are often slightly misoriented. Similar, small misorientations exist between adjacent clay packets within the coatings at distance from the glass surface. Interfaces between adjacent packets are grain boundaries consisting of arrays of edge dislocations. Larger layer silicate laths occur sporadically in this sample (Figure 10). These can be identified as muscovite-like, based on their diffraction patterns (see inset in Figure 10 indicating a group A (Bailey 1988) polytype) and K-aluminosilicate compositions. However, the K contents are lower than that of unaltered muscovite. Note that the 20*l* rows in the SAED pattern show streaking parallel to c^*. Lattice fringe images from laths show occasional layers with modified contrast (inset in Figure 10). The lath is surrounded by topotactic overgrowths and more randomly oriented packets of clay (lower left corner of Figure 10), as

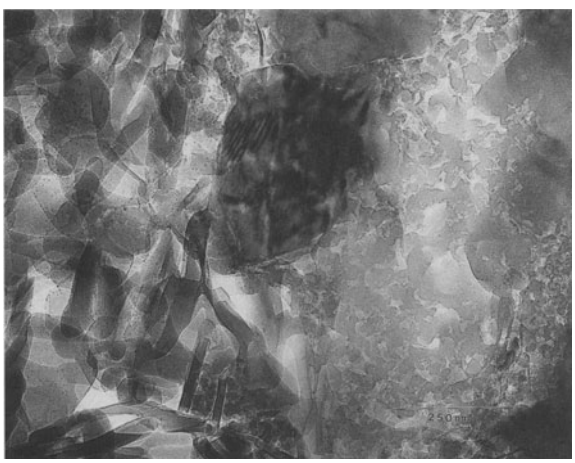

Figure 6. TEM of glass (top right), zeolites (tabular crystals mostly on the left), opal-like silica and etched glass (center and right). A small, twinned, essentially unweathered crystal of K-feldspar (dark contrast center top) is shown (sample G4 1531).

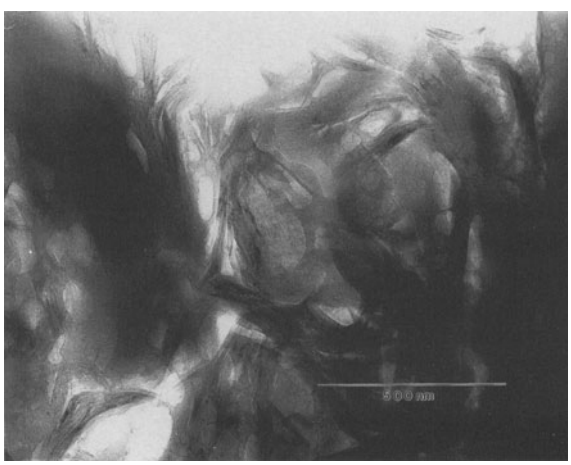

Figure 8. TEM of porous, corroded glass containing rounded solution pits (left) and abundant smectite, especially at external surfaces (sample GU3 1406).

https://doi.org/10.1346/CCMN.1998.0460104 Published online by Cambridge University Press

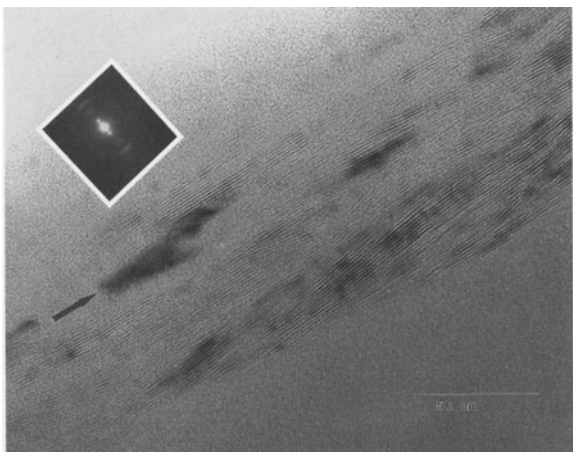

Figure 9. High-resolution TEM of smectite and included oriented Fe-oxyhydroxide crystal (arrowed) developed on a corroded glass surface in sample GU3 1406. The selected area electron diffraction pattern shows the ~1.0-nm basal spacing of the clay and streaking along 02*l*, indicating disordered stacking. Subparallel packets of smectite a few layers thick are separated by arrays of edge dislocations.

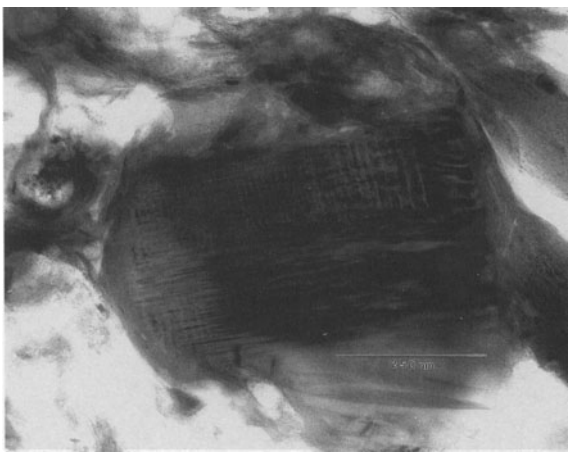

Figure 11. TEM image of a highly weathered region of sample GU3 1406 showing extensive replacement of glass by clays. The small, microcline twinned alkali feldspar crystal (center) is essentially unaltered, but coated by smectite that has nucleated on its surface.

well as elongate crystals of Fe-oxyhydroxide (probably goethite, see below).

Small, submicron-diameter K-feldspar crystals in the groundmass show microcline twinning (Figure 11). Interiors of these crystals are always essentially unaltered and surfaces show few signs of etching or dissolution. However, their surfaces are generally coated by clay minerals.

Secondary product assemblages consist of intimate mixtures of Fe-oxides and clays (Figure 12). The clays are characterized by a 1-nm basal spacing. The few tens of nanometers wide, Fe-rich, elongate particles enclosed by clays in Figure 12 (dark contrast) display 1.0-nm lattice fringes parallel to their length. Compositional and diffraction data are consistent with identification of this phase as goethite. In many cases, goethite is topotactically oriented, with b^* goethite parallel to c^* clay.

Some regions of glass contain dispersed hematite crystals, identified by their SAED patterns and composition. In other regions, hematite coexists with goethite in aggregates of glass alteration products (Figure 13). In general, Fe-oxide particle sizes range from nanocrystalline (few-nanometers-diameter) to a fraction of a micron.

Manganese-rich minerals are also present. Figure 14a illustrates etched glass (note rounded solution pits)

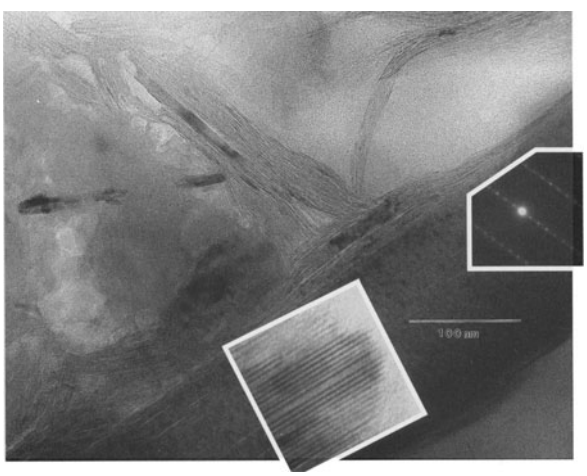

Figure 10. High-resolution TEM of illitized muscovite (lower right) surrounded by smectite and an elongate goethite crystal (thin, dark crystal center left) in sample GU3 1406. Insets show a more highly magnified lattice fringe image and [010] SAED pattern from this crystal.

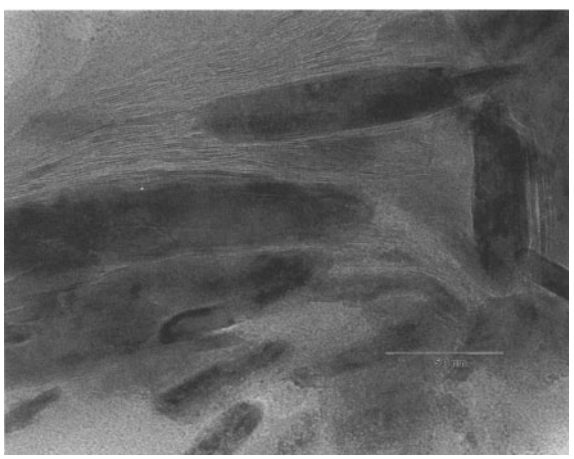

Figure 12. Lattice fringe TEM showing that smectites commonly contain few tens of nanometers wide, elongate goethite crystals (darker contrast), often in topotactic orientations (sample GU3 1406). HRTEM micrograph.

https://doi.org/10.1346/CCMN.1998.0460104 Published online by Cambridge University Press

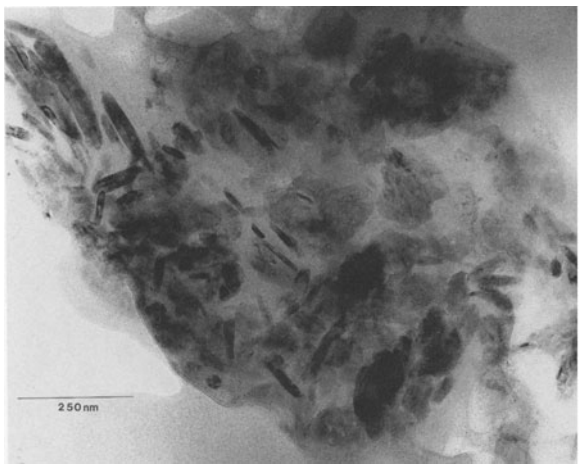

Figure 13. TEM showing aggregates of finely crystalline Fe-oxides and Fe-oxyhydroxides (dark particles) in altered glass in sample GU3 1406.

Figure 15. Low-magnification TEM image of abundant groundmass feldspars in G4 272 showing very little evidence for alteration except at grain boundaries. The contrast within alkali feldspars is due to semi-periodic, twinned, albite exsolution lamellae.

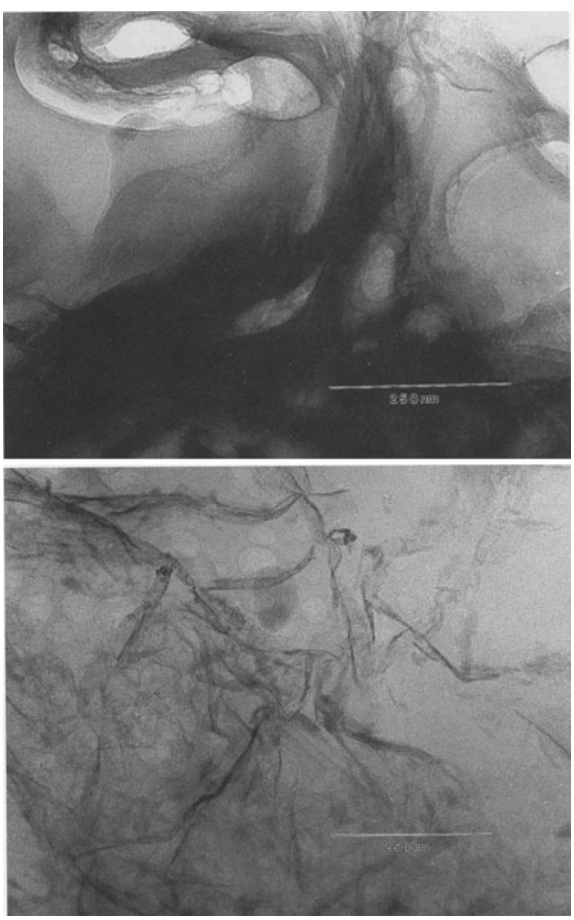

Figure 14. TEM showing (a) smectite growing from corroded glass surfaces in sample GU3 1406. The upper surface of the clays is coated with a Mn-oxyhydroxide. The filmy Mn-oxyhydroxide is shown in (b).

covered by clay minerals. The outer surface of the glass-clay assemblage consists of filmy Mn-oxide (upper Figure 14a, shown in detail in Figure 14b).

GSW G4 272 Topobah Springs Member

Feldspar phenocrysts in a groundmass of micron-sized alkali feldspar dominate the primary mineralogy and secondary mineral assemblage in sample GSW G4 272. At low magnification, micron-sized groundmass feldspars exhibit typical microstructures due to fine-scale structure modulation and (010) exsolution (Figure 15). Na-rich exsolution lamellae are albite twinned. Alteration is generally confined to narrow grain boundaries (Figures 15 and 16) and cracks (Figures 17, 18 and 19). The dislocation array at the bot-

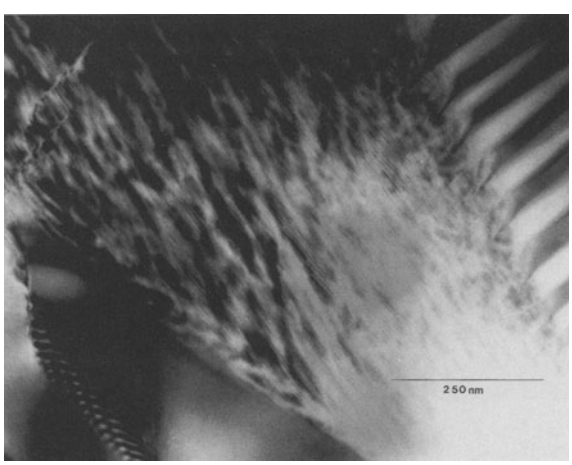

Figure 16. TEM illustrating groundmass feldspars in G4 272. Grain boundaries and dislocations (lower left) are essentially unaltered.

https://doi.org/10.1346/CCMN.1998.0460104 Published online by Cambridge University Press

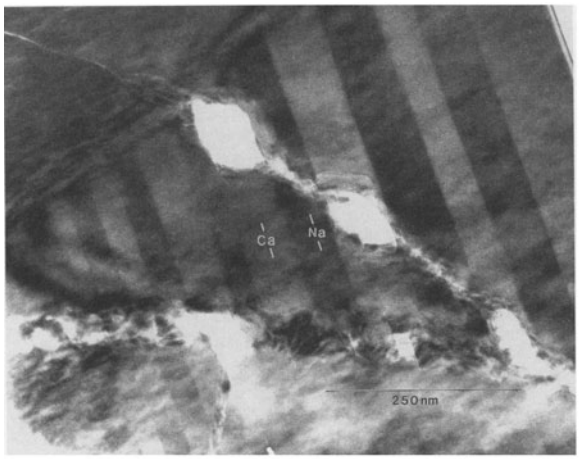

Figure 17. TEM illustrating dissolution features in groundmass feldspars in G4 272. Alkali feldspar (top left) shows no alteration. Exsolution lamellae in plagioclase that are richer in Ca (light contrast, labelled "Ca") show significant dissolution focused at crack surfaces compared to albite-rich lamellae (labelled "Na").

Figure 19. TEM illustrating K, Na-bearing aluminosilicate particulate, gel-like material (arrowed) adjacent to alkali feldspar surfaces in G4 272.

tom left and top left of Figure 16 shows only very minor etching.

Figure 17 is a region of groundmass feldspar consisting of exsolved Ca, Na, K feldspar (bottom and top right) and modulated alkali feldspar (top left). The region contains a grain boundary and 2 cracks, one of which cuts both feldspar crystals. The grain boundary between exsolved and modulated feldspar is essentially unaltered, as is the region around the crack within the Na-K feldspar. Large etch pits along both cracks are confined to low-contrast lamellae, which are richer in Ca-rich.

The most common secondary material in this sample, a very poorly crystalline or amorphous phase, is normally only developed in cracks and at grain boundaries. Figure 18 illustrates an ~70 nm wide grain boundary coated with spherical particles of aluminosilicate. Individual particles are typically ~5 nm in diameter. Note that dislocations in this region are unetched.

In some areas, small quantities of porous, apparently amorphous subspherical aluminosilicate particles occur at surfaces of feldspars (Figure 19). The composition of this material resembles that of feldspar. In some cases, there appears to be a continuum between feldspar and particulate alteration products (Figure 20). Occasionally, few-nanometers-wide clay strips occur in this material.

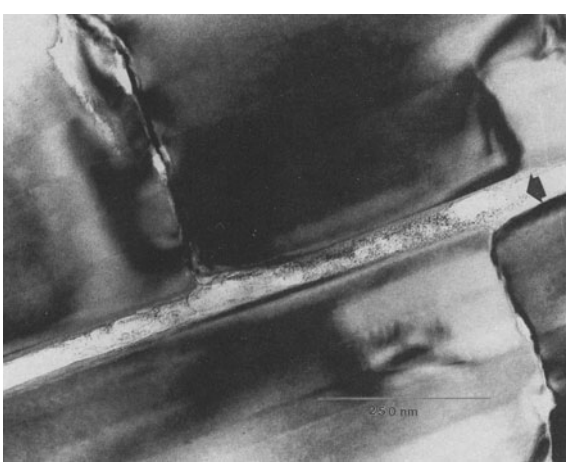

Figure 18. TEM showing a crack in alkali feldspars in G4 272 partially coated by a granular, apparently amorphous Na-K-bearing aluminosilicate (arrowed).

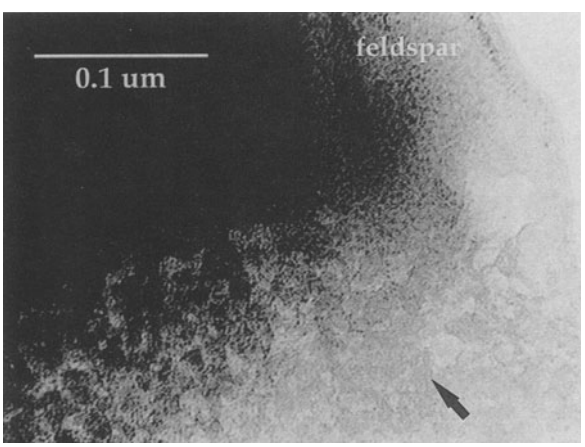

Figure 20. TEM showing details of the interface between aluminosilicate gel-like material and the feldspar surface showing gradual transition from particulate alteration products (arrow) to etched feldspar.

https://doi.org/10.1346/CCMN.1998.0460104 Published online by Cambridge University Press

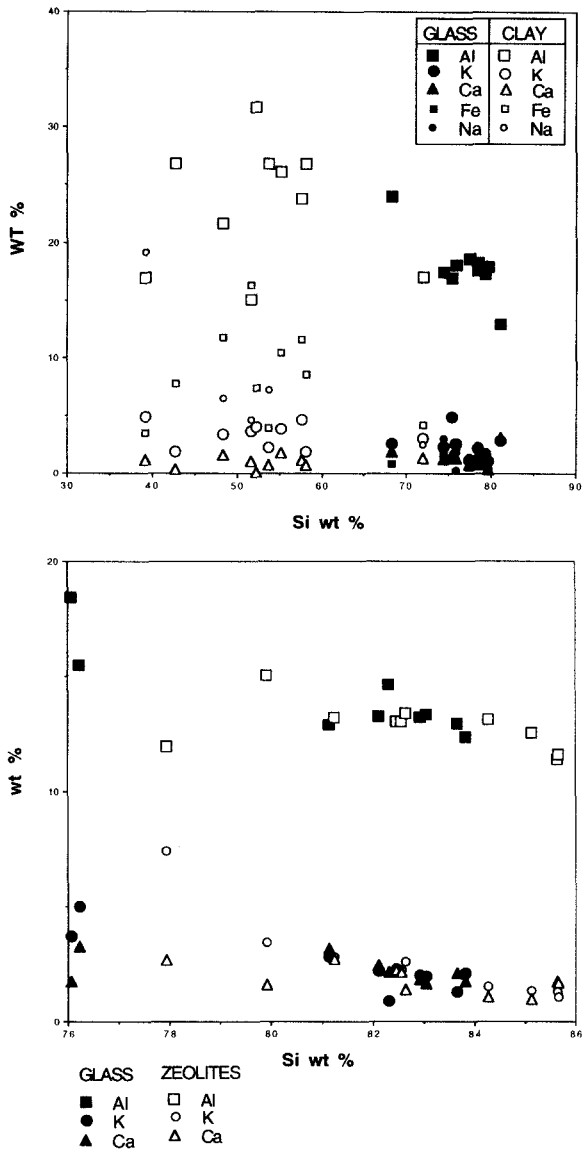

Figure 21. Semiquantitative AEM data: a) illustrating the differences in composition between glass and clays in GV 1406; b) comparing the compositions of zeolites and associated glass in GV 1531.

Comparison Between Compositions of Glass, Clay and Zeolites

AEM analyses were collected from glass and its abundant alteration products. Absolute weight percentages are not accurate due to uncertainties in the K-factors. This does not affect comparison between data from glass and alteration products as the same correction factors were used for all analyses. Compositional data from glass and associated clay (G4 1406) that indicate clays are slightly enriched in Al, significantly poorer in Si, enriched in Fe and have similar K and Ca contents (Figure 21a). Clays also contain some Mg, Ti, Mn and Zn.

The compositions of zeolites and glass are both quite variable (Figure 21b). However, zeolite compositions are closely similar to those of the glasses from which they formed.

DISCUSSION

TEM data from the 3 samples examined in this study reveal degrees of alteration ranging from minimal in the devitrified, alkali feldspar-dominated sample of the Topobah Springs Member to extensive in the glass bearing samples from the Calico Hills formation. Assemblages of smectite, zeolites and spongelike aggregates of nanocrystalline aluminosilicate spheres found in this study are in general agreement with previous work on alteration of tuffaceous ash layers (Bohor and Triplehorn 1993). Lack of alteration of groundmass feldspars is important due to the possibility that their secondary products may have contributed to adsorption measured in laboratory studies (Meier, personal communication, 1995).

Alteration of Yucca Mountain Tuffs—Calico Hills Formation

Zeolitization in Yucca Mountain tuffs is generally attributed to a hydrothermal event associated with nearby volcanic activity which occurred between 10 and 11 million years ago (Bish and Aronson 1993).

Carlos et al. (1995) reported that a sample from the zeolitic part of the Calico Hills formation contained abundant mordenite $(Ca,Na_2,K_2)Al_2Si_{10}O_{24}{\cdot}7(H_2O)$ and lesser amounts of clinoptilolite $(Na,K,Ca)_{23}Al_3(Al,Si)_2Si_{13}O_{36}{\cdot}12(H_2O)$. Although these phases were not distinguished in our study, their coexistence may account for the dispersion in Al:Si in our zeolite analyses (Figure 21b).

Our results for sample G4 1531 reveal what appears to be a continuum in structural and morphological states between glass, etched glass, glass showing an irregular semi-fibrous morphology and fibrous zeolites. Based on this, and the compositional similarity between coexisting zeolites and glass, we suggest that zeolites form predominantly by glass restructuring or recrystallization rather than by large-scale dissolution–reprecipitation. This differs from previous hypotheses (such as Broxton et al. 1987), which advocate precipitation of zeolites from solution onto etch pit surfaces. The apparent discrepancy may be due to the focus of previous studies on fracture coatings, which may form by different processes than matrix zeolites examined in this study.

Sample G4 1531 comes from diagenetic zone II (Broxton et al. 1987). Broxton et al. (1987) reported zeolite compositions were considerably more calcic than the associated glass. However, AEM data in Figure 21b show a relatively high degree of similarity in

https://doi.org/10.1346/CCMN.1998.0460104 Published online by Cambridge University Press

K,Ca contents and Al:Si of zeolites and immediately adjacent glass. Thus, our data suggest that glass compositions may play a role in determining the composition and structure of associated zeolites.

Etched surfaces, rounded solution pits and aggregates of few-nanometers-diameter silica-rich particles (tentatively identified as opal-CT) characterize altered glass in G4 1531. It is unlikely that the extremely small, possibly noncrystalline or highly defective silica-rich particles could have survived elevated temperatures for any length of time without coarsening and recrystallization. Thus, we suggest the opal-like silica formed at close to current ambient temperatures. The topography of altered glass surfaces suggests that formation of opal-like material involves subdivision of the glass surface by etching. This may be followed by reaggregation of the porous, probably hydrated, sponge-like glass material to form spherical particles, probably to lower surface energy (see Figures 2 and 6). Alternatively, opal-like silica may form simply by reprecipitation of dissolved silica or by a combination of these processes.

Minor clays occur in G4 1531. The ~1.0-nm basal spacing and complex chemistry are broadly consistent with smectite (dehydrated in the vacuum). The interlayer K may indicate some intergrowth with illite. While in theory it is possible to distinguish illite from smectite using contrast in overfocused images (Guthrie and Veblen 1990), this is impractical for particles no more than a few unit cells in thickness. In some cases, smectite-like clays occur as thin mineral coatings or as few unit cell wide ribbons within the opal-like phase. Clays probably contain a fraction of the Al, Fe and other elements released by glass dissolution and not accommodated in the opal CT-like phase.

Figure 10 illustrates a partially weathered muscovite lath. Streaking along reciprocal lattice rows parallel to c^* is probably due to randomly interstratified layers with a different chemistry and/or structure. At higher magnification, these individual modified layers can be observed (inset in Figure 10). Because intergrowths of the modified layers and muscovite occur at the unit-cell scale, it is not possible to quantitatively determine the exact composition of the clay. Based on ~1-nm basal spacing and low K content of the lath compared to unaltered muscovite, the clay is probably illite.

K-feldspar crystals in both samples of the Calico Hills formation are generally micron to submicron in diameter. Although authigenic K-feldspar might be anticipated as an alteration product of glass (Broxton et al. 1987), crystals show well-defined microstructures indicating relatively high temperature crystallization. No development of reaction products at internal sites was detected. However, crystals are commonly coated by smectite-like clays with their basal planes parallel to feldspar surfaces. Because the feldspar crystal surfaces are essentially unetched, it is likely that clays formed from constituents released by the surrounding extensive glass alteration reactions. The surface parallel orientation of clays may arise because smectite nucleated from cations and water adsorbed onto the mineral surface.

Glass surfaces in sample GU3 1406 of the Calico Hills Formation are often intimately associated with clay minerals. These are observed both to grow outward from surfaces and to develop with their basal planes parallel to surfaces. The complex chemistry (especially the mixture of interlayer cations), morphology and basal spacing of the clay is consistent with smectite. Data indicate the most important compositional change that accompanies formation of smectite from the glass is loss of Si. Thus, smectites are comparatively Si-poor and slightly enriched in Al and Fe as well as minor constituents such as Mg, Ti, Mn and Zn compared to glass.

In some regions, no porosity exists at interfaces between smectite-like clays and glass (Figure 9), suggesting that clay growth is fast enough to consume elements and space generated by glass dissolution. Thus, clay growth at the clay–glass interface probably involves a small loss of silica and limited scales of transport of silica and metals retained in the smectite structure. In other regions (Figure 7), smectite growth has not occurred over the entire surface, implying larger loss of glass constituents to solution.

Microstructures in glass coatings are sometimes complex, especially in coatings where basal planes of smectite parallel glass surfaces. Figure 9 illustrates numerous subgrain boundaries (collections of edge dislocations) that separate <10 unit cell wide packets of smectite. At the glass surface, it is common to observe that adjacent regions of smectite are slightly misoriented with respect to each other. As smectite orientation is dictated by the orientation of the underlying glass surface, this is interpreted to reflect nonparallelism of etch pit bottoms throughout the time that the parallel packets of smectite layers formed. This suggests that discontinuities throughout the coating reflect discontinuous, heterogeneous retreat of the surface. Such episodic changes may be attributed to seasonal or other factors.

In several studies, Mn-oxides have been reported in association with fracture coatings in these tuffs (for example, Carlos et al. 1993). Our results indicate that these sometimes occur as films on clay surfaces, suggesting Mn-oxide formation occurred relatively late in the alteration history.

Differences in Weathering Products of G4 1531 and GU3 1406

The presence of preexisting zeolites and associated porosity and permeability clearly evident in electron micrographs (Figures 1–4) may have influenced subsequent low-temperature alteration of the tuffs. Fluid

https://doi.org/10.1346/CCMN.1998.0460104 Published online by Cambridge University Press

flow in zeolitized tuffs should be faster than in non-zeolitized units. Furthermore, as the samples are from above the current water table, the residence time for bulk water should be less and solutions may be more dilute. This may explain why the assemblage of secondary minerals in the zeolitized sample is dominated by opal-like silica (a product of glass dissolution) and in the unzeolitized sample by more compositionally complex smectites that form by nucleation and growth at glass surfaces.

AEM data show compositional differences in glasses in these 2 members of the Calico Hills formation. Notably, glass in GU 1406 is more aluminous and slightly richer in Fe. This may also contribute to differences between glass alteration assemblages in the 2 samples.

Alteration of Yucca Mountain Tuffs—Topobah Spring Member

Alkali feldspar is the predominant phase in this devitrified tuff. Crystals exhibit complex microstructures (exsolution and twinning) consistent with relatively high-temperature origins. The small particle size of groundmass feldspars generates abundant grain boundary area.

TEM data show grain boundaries and cracks to be the reactive dissolution sites, particularly along cracks in more calcium-rich lamellae. Note that about 4 to 6 times more material appears to have been removed from Ca- compared to Na-rich lamellae (Figure 17). This suggests a difference in dissolution rates of about half an order of magnitude. K-rich feldspar is apparently at least an order of magnitude less reactive than either plagioclase. The general order of reactivity agrees with most previous field-based studies of feldspar dissolution but is inconsistent with experimental measurements (see Blum and Stillings 1995 for discussion).

In rare areas, TEM data reveal poorly crystalline or amorphous, silica-rich materials. The origin of this material is unknown. Observations such as the association of nanoscale particles with feldspar surfaces that are complexly corroded on the nanometer scale suggest that this material formed by etching and restructuring at the feldspar surface. However, it is also possible that it formed from glass alteration or by precipitation of material introduced in solution.

Coatings and Contaminant Transport

A full analysis of transport requires 3-dimensional information about porosity, permeability, pore size distribution, surface area and mineralogy. In many contaminant transport studies, much of this information is available. However, these measurements are not available for the samples examined here. Values are available for 3 samples of G4 1548 that are similar to G4 1531 (but from approximately 5.2 m away). Hydraulic conductivities are $<1.31 \times 10^{-11}$, 5.9×10^{-12} and 5.72×10^{-9} m/s (intrinsic permeabilities: $<1.36 \times 10^{-6}$ darcy, 6.13×10^{-7} darcy and 2.05×10^{-6} darcy) and porosities are 0.27, 0.28 and 0.32 (data from Loven, written communication Bish 1997). Another sample from close to G4 1531, G4 1511, has a hydraulic conductivity of 5.72×10^{-9} m/s (intrinsic permeability of 5.95×10^{-4} darcy) and a porosity of 0.32. The combination of relatively low (but variable) hydraulic conductivity with high porosity (compared to values tabulated by Spitz and Moreno 1996) probably reflects the extremely small pore size (often sub 0.1 μm diameter) associated with interpenetrating zeolite needles.

Sample GU3 1440 (similar to GU3 1408) has a hydraulic conductivity of 2.68×10^{-7} m/s (intrinsic permeability of 2.79×10^{-2} darcy) and a porosity of 0.45 (data from Loven, written communication Bish 1997). The high porosity and hydraulic conductivity (compared to zeolitized samples) is consistent with the open space associated with glass dissolution, evident in electron micrographs of this sample.

What is often unknown in contaminant transport studies is the nature of reactive grain coatings developed as the result of low-temperature chemical reactions. These are generally inferred to be very important in controlling elemental distribution because the coatings consist of very finely crystalline or amorphous phases that present large amounts of reactive surface area to solution. Models and analysis of laboratory data for contaminant behavior in tuffs from Yucca Mountain require knowledge of the mineralogy and physical state of altered tuffs, including details such as the form and distribution of fine-grained products provided here. Our results show that particle sizes of alteration products range from few-nanometers to submicron. Smectites, oxides and oxyhydroxides may be important in controlling element mobility. In addition to the effects of their high surface area due to extremely small particle size, smectites can modify element distributions through cation exchange in interlayer sites. In combination, these factors suggest that smectites and other alteration products may have an effect far greater than expected based on their volume percentage abundance, as determined by XRD studies.

Silica-rich alteration products are finely divided and arranged into approximately randomly packed aggregates. These porous aggregates are characterized by abundant nanoscale porosity and probably enclose small volumes of solution with chemistries very different to that of bulk fluid. Thus, silica surfaces and microenvironments within particle clusters may affect contaminant distribution and transport in these rocks.

It was noted at the time the decision was made to investigate the Yucca Mountain as a potential site for the high-level nuclear waste repository that zeolites have a substantial ability to affect cation mobility

(Johnstone and Wolfsberg 1980). Recent studies have shown that, although they can effectively immobilize radionuclides, their ability to retain actinides is limited (Triay et al. 1991; Vaniman and Bish 1993). Our data show that the zeolites should also impact contaminant transport through their effect on the structure of porosity and via adsorption due to high surface areas.

Despite relatively low cation exchange capabilities, Mn-oxides show strong retardation capabilities for transuranic elements (such as U, Np, Pu, Am; Carlos and Chipera 1990; Triay 1991; Triay et al. 1991; Carlos et al. 1993, 1995). Carlos et al. (1993) reviewed the mechanisms by which adsorption occurs. In the Calico Hills Formation, the Mn-oxides occur as very thin films coating altered surfaces. Thus, their morphology is optimized for surface adsorption of these elements from solution.

In addition to cation exchange and surface adsorption considerations, the mineralogy is important in understanding the long-term response of these tuffs to thermal and hydrologic changes associated with heat generated by radioactive decay in the nuclear waste repository (Bish et al. 1982; Blacic et al. 1986; Bish 1988). The rates of these reactions will depend on the form and distribution of minerals. Data presented here reveal details of how reactive phases are distributed; provide insight into how zeolites, clays and silica phases form; and indicate types of physical and chemical changes that may occur in these tuffs in the future.

ACKNOWLEDGMENTS

Thanks are expressed to I. Triay and her colleagues at Los Alamos National Laboratory for providing samples and some funding to support this research, to D. Bish for providing some of the relevant data and publications and to L. Kovack for additional information. The manuscript benefited from the constructive criticisms of J. Post and 2 anonymous reviewers. Funding for this research was also provided by National Science Foundation grant number EAR9317082.

REFERENCES

Bailey SW. 1988. X-ray identification of the polytypes of mica, serpentine, and chlorite. Clays Clay Miner 36:193–213.

Barker WW, Banfield JF. 1996. Biologically- versus inorganically-mediated weathering reactions: Relationships between minerals and extracellular microbial polymers in lithobiontic communities. Chem Geol 132:55–69.

Bish DL. 1988. Smectite dehydration and stability: Applications to radioactive waste isolation at Yucca Mountain, Nevada. Los Alamos Natl Lab Report LA11023MS.

Bish DL, Aronson JL. 1993. Paleogeothermal and paleohydrologic conditions in silica tuff from Yucca Mountain, Nevada. Clays Clay Miner 41:148–161.

Bish DL, Chipera SJ. 1989. Revised mineralogic summary of Yucca Mountain, Nevada. Los Alamos Natl Lab Report LA11497MS. 68 p.

Bish DL, Vaniman DT, Byers FM, Broxton DE. 1982. Summary of the mineralogy-petrology of tuffs of Yucca Mountain and the secondary-phase thermal stability in tuffs. Los Alamos Natl Lab Report LA9321MS.

Blacic JD, Vaniman DT, Bish DL, Duffy CJ, Gooley RC. 1986. Effects of long-term exposure of tuffs to high-level nuclear waste repository conditions. Final Report. Los Alamos Natl Lab Report LA9330MS.

Blum AE, Stillings LL. 1995. Feldspar dissolution kinetics. In: White AF, Brantley SL, Editors. Chemical weathering rates of silicate minerals. Rev Mineral 31:291–351.

Bohor BF, Triplehorn DM. 1993. Tonsteins: Altered volcanic-ash layers in coal bearing sequences. Geol Soc Am Spec Paper 285. 44 p.

Bolivar SL, Broxton DE, Bish DL, Byers FM, Carlos BH. 1989. Mineralogy–petrology studies and natural barriers at Yucca Mountain, Nevada. Nuclear waste isolation in the unsaturated zone: FOCUS '89; Las Vegas, NV; 18–21 Sep 1989. LAUR892952, CONF8909283.

Broxton DE, Bish DL, Warren RG. 1985. Distribution and chemistry of diagenetic minerals at Yucca Mountain, Nye County, Nevada. DOENBM7013292.

Broxton DE, Bish DL, Warren RG. 1987. Distribution and chemistry of diagentic minerals at Yucca Mountain, Nye County, Nevada. Clays Clay Miner 35:89–110.

Carlos BA, Bish DL, Chipera SJ. 1990. Manganese-oxide minerals in fractures of the Crater Flat Tuff in drill core USW G-4, Yucca Mountain, Nevada. Los Alamos Natl Lab Report LA11787MS. 61 p.

Carlos BA, Chipera SJ, Bish DL. 1995. Distribution and chemistry of fracture-lining minerals at Yucca Mountain, Nevada. Los Alamos Natl Lab Report LA-12977-MS. 92 p.

Carlos BA, Chipera SJ, Bish DL, Craven SJ. 1993. Fracture-lining manganese oxide minerals in silicic tuff, Yucca Mountain, Nevada, U.S.A. Chem Geol 107:47–69.

Chipera SJ, Bish DL. 1989. Quantitative X-ray diffraction analyses of samples used for sorption studies by the Isotope and Nuclear Chemistry Division, Los Alamos Natl Lab. Los Alamos Natl Lab Report LA-11669-MS. 20 p.

Coston JA, Fuller CC, Davis JA. 1995. Pb^{2+} and Zn^{2+} adsorption by a natural Al-and Fe-bearing surface coating on an aquifer sand. Geochim Cosmochim Acta 59:3535–3547.

Guthrie GD, Veblen DR. 1990. Interpreting one dimensional high-resolution transmission electron micrographs of sheet silicates by computer simulation. Am Mineral 75:276–288.

Johnstone JK, Wolfsberg K. 1980. Evaluation of tuff as a medium for a nuclear waste repository: Interim status report on the properties of tuff. Sandia Natl Lab Report: SAND80-1464. 134 p.

Spitz K, Moreno J. 1996. A practical guide to groundwater and solute transport modeling. New York: J Wiley. 461 p.

Thomas KW. 1987. Summary of sorption measurements performed with Yucca Mountain, Nevada, tuff samples and water from Well J-13. Los Alamos Natl Lab Report LA-10960-MS. 99 p.

Triay IR. 1991. Radionuclide migration as a function of mineralogy. 2nd Annu High-Level Radioactive Waste Mgmt Conf; Las Vegas, NV. cited in Carlos et al. 1993.

Triay IR, Mitchell JA, Ott MA. 1991. Radionuclide migration as a function of mineralogy. Proc. 2nd Annu High-Level Radioactive Waste Mgmt Conference; Las Vegas, NV. p 494–498.

Vaniman DT, Bish DL. 1993. Importance of zeolites in the potential high-level radioactive waste repository at Yucca Mountain, Nevada. Zeolite 93: 4th Int Conf on the Occurrence, Properties, and Utilization of Natural Zeolites; Boise, ID; 20–28 Jun 1993. LAUR932326, CONF93061002.

(Received 3 December 1996; accepted 15 April 1997; Ms. 2834)